VALIDATION OF THE USGS SENSOR MODEL FOR TOPOGRAPHIC MAPPING OF VENUS USING MAGELLAN RADAR STEREOIMAGERY. E. Howington-Kraus, R. Kirk, D. Galuszka, T. Hare and B. Redding, United States Geological Survey, Astrogeology Team, Flagstaff AZ 86001, (email: ahowington@usgs.gov).

Introduction: The Magellan spacecraft went into Venus orbit in 1990 and by 1992 had made three complete cycles of polar orbits, each cycle covering the full range of longitudes. During this time the spacecraft obtained synthetic aperture radar (SAR) images of >96% of the planet at a resolution of 75 m/pixel [1]. Images taken with a decreased look angle from vertical, primarily during Cycle 3, provide stereo coverage of 17% of the planet when combined with images with same-side illumination from earlier in the mission. The stereo geometry of these images is extremely favorable, allowing elevation measurements with an estimated vertical precision (EP) of ~10 m [2]. Magellan also obtained radar altimetry data at a horizontal resolution of 10x25 km, but photogrammetric analysis of the stereoimagery can yield topographic maps with a horizontal resolution more than an order of magnitude superior to that of the altimeter.

Due to the volume of data (~30 Gbytes) in the same-side stereo coverage of Venus, digital (or softcopy) photogrammetic systems have been developed to stereoscopically derive Magellan digital elevation models (DEMs). After working with two such systems, the Magellan Stereo Toolkit (MST) developed by VEXCEL [3] and the SAIC Digital SAR Workstation-Venus (DSW-V) [4], we undertook the development of software needed to utilize Magellan stereomagery on the commercial digital photogrammetric workstation that we use for mapping with a variety of other planetary datasets. The special hardware and SOCET SET software [5,6] of this system (an LH Systems DPW 790) provide many useful capabilities for mapping, including import/export of common data formats, bundle-block adjustment, automatic extraction of DEM data, stereo display and interactive editing of DEMs, orthophoto generation and mosaicking, and image display and enhancement tools. These capabilities can be extended by programming with the SOCET SET Developer's Toolkit (DEVKIT). We have written programs to import planetary images and supporting data from ISIS [7,8,9], which is used for mission-specific data ingestion and calibration steps into SOCET SET for stereomapping. Such translation software gives us the ability to do topographic mapping with data from missions such as Mars Pathfinder [10], Clementine [11], Viking [12] and Mars Global Surveyor [13]. The unique properties of the Magellan SAR data made it necessary to develop both translation software and a sensor model [14].

Sensor Model: A sensor model is a function that specifies the transformation between image space (lines, samples) and object or ground coordinates (latitude, longitude, elevation). In addition to the image-to-ground function and its inverse (one of the two can be implemented numerically, given the other) a complete sensor model for SOCET SET contains 9 other functions, most of which carry out data input/output and bookkeeping functions.

Our Magellan SAR sensor model (which is based on the sensor model utilized by the SAIC DSW-V) includes all the physics of the Magellan imaging process, and accounts for the fact that during the Magellan imaging process, the images have been partially orthorectified as part of the correlation process: distortions attributable to topography were removed (but only those accounted for in the very low resolution pre-Magellan topo model) and must be put back in for the images to be matched correctly. Specifically, for a given ground point, the sensor model first determines which orbit strip (BIDR) the ground point is contained in, and then which radar burst from that BIDR. Once the radar burst is identified, the burst resampling coefficients and spacecraft position and velocity at the time of observation are known. Second, the range and doppler coordinates that the ground point was observed at are then calculated based on the spacecraft position and velocity at the time of observation. (This is the physical process of image formation that we must model.) In addition, the computed coordinates are corrected for atmospheric refraction. Finally, the resampling coefficients associated with the burst are applied to the range and doppler coordinates to determine the image coordinates ("C1-C2" or line and sample) at which this range-doppler point was put into the image.

The software is designed to work with any combination of unmosaicked (F-BIDR), Mission-mosaicked (F- and C-MIDR), and USGS-mosaicked (FMAP) images. Our translator programs import these different formats into a single SOCET SET Magellan image format that can contain data from any number of orbits. A database (built from the BIDR libraries on tape and CD-R) provides the footprint of each orbit and burst in the image and the radar parameters needed for the sensor model calculations. Information about the spacecraft position and velocity can be taken either from the F-BIDRs or from separate NAIF SPICE kernels, letting us take advantage of post-mission improvements to the spacecraft ephemerides without the need to redo SAR correlation or mosaicking. In addition, the SOCET SET bundle-adjustment software can be used to estimate corrections to the ephemeris of each orbit. The form of the corrections, offsets and velocity adjustments in three orthogonal directions (along-track, across-track, and radial) suffices to correct the orbits over short arcs and reconcile SAR and altimetry observations.

Initial Test Results: Experimentation on three subsets of Magellan stereo data demonstrated the ca-

pability and speed of the DPW system [14] and allowed us to develop effective procedures for operational mapping, but unfortunately also exposed some significant problems. The first test used images of the stereo test area acquired during Cycle 2 of the Magellan mission, which we previously used to test the SAIC DSW-V and the VEXCEL MST systems. The SOCET SET matcher was found to combine the high speed of automatic matching available in MST with high DEM resolution, but some manual editing was necessary in very bland image areas.

Development of procedures for control and stereomatching required a larger dataset, such as the 64 Cycle 1 and 53 Cycle 3 orbits covering FMAP quadrangle 06S066 (Joliot-Curie). We were particularly concerned with the well-known "cliffs," artifacts in the stereo data caused by discrepancies between the mission ephemeris solutions for successive blocks of orbits. Alex Konopliv of JPL reprocessed the entire set of orbital tracking and navigation data based on the detailed gravity observations from the end of the mission and claimed that errors in the new orbit solutions were decreased 1.5 orders of magnitude (to 50-200 m) in all 3 axes [15]. Our test mapping unfortunately showed that errors of this magnitude north-south interfered with stereomatching, while east-west ephemeris errors resulted in height offsets in the derived stereomodels. To produce seamless elevation data, we found it necessary to collect image-to-image tiepoint measurements and use these to estimate 3-axis corrections to the orbits as described above. Correcting the Konopliv ephemerides in this way yielded solutions in good agreement with Magellan altimetry. Correcting the mission ephemerides eliminated relative errors (seams) between stereomodels but did not correct the absolute positional errors present in the earlier solution. Thus, both the improved orbit/tracking solution and corrections based on the images themselves are necessary ingredients for successful stereomapping.

A second result of the Joliot-Curie tests was the development of a stereomatching procedure that minimized the need for manual editing of the final results. By itself, the SOCET SET matching software had limited success following the extremely rugged terrain of the venusian highlands. We found that "seeding" the DEMs with a small number of manually collected points on ridge and valley lines greatly improved the success rate of the automatic matching step. With this approach, the need for manual editing was largely limited to bland areas where the matcher failed entirely. In a few areas of intermediate roughness, however, the matcher did not fail but produced artifacts in the form of roughly east-west trending bands superimposed on the real topography. The cause of these artifacts is discussed below.

A third test area covering Maxwell Montes was selected because of the availability of an independent set of improved ephemerides, calculated by Paul Chodas of JPL, based on his own tiepoint measurements [16]. Our experience in Joliot-Curie suggested that Chodas's tiepoint-based solution would probably be usable for mapping without further bundle adjustment, but that it might not have the absolute accuracy of the Konopliv solution. Unfortunately, we were not able to map this area because of what appeared to be a large (several km) offset between Cycle 1 and Cycle 3 images in this region. With the two images of each stereopair misaligned by this amount, automatic matching was not possible. Although it would be possible to bring the images into alignment by bundle adjustment, we considered it essential to first understand the cause of the large discrepancy.

Coordinate Errors Resolved: Further investigation of the offset discovered in the Maxwell images yielded some puzzling clues. We found that the C1 (north-south) coordinates of burst centerpoints computed in our software differed from the values stored in the F-BIDR headers and that this discrepancy varied in a smooth but complex way along each orbit. The pattern of small discrepancies at low latitudes and larger (up to 2 km, or 15 pixels) discrepancies at high latitudes explained our success in mapping Joliot-Curie and failure near Maxwell. We eventually found the main cause of the error to be a simple bug in the sensor model code (inherited from the SAIC DSW-V): doppler frequencies were being computed based on the nominal radar wavelength of 12.6 cm instead of the exact wavelength 12.5699161… cm. Using the correct wavelength reduced the maximum coordinate discrepancies at high latitudes to <2 pixels (0.15 km) and eliminated the previously mentioned east-west artifacts in the low latitude DEMs as well as minor "jumping" of the cursor in the interactive stereo display. The remaining discrepancy in C1 coordinates was traced to the difference between implementations of the atmospheric refraction correction in our software and in the Magellan SAR processor that produced the F-BIDRs. Both software packages use a simple empirical function fit to numerical calculations of atmospheric refraction. It seems likely that the SAIC/USGS calculation, which uses a rational function of ground point elevation, spacecraft elevation, and their horizontal separation, is slightly more accurate than the SAR processor code, which uses a polynomial in spacecraft elevation and horizontal separation only. Nevertheless, we have adopted the Magellan SAR processor refraction code in our sensor model in order to insure

that our DEMs are positionally consistent with the mission-produced images.

Validation of Control Procedures: Although the errors and discrepancies in ground coordinate calculations were accounted for and the procedures needed for operational topographic mapping of Venus with the Magellan images were available, there were still some lingering concerns over the bundle adjustment process. The adjustment calculation takes as input both the coordinates of selected features (pass-points) in the images and interpolated altimetry data; the resulting corrections to the ephemerides are intended not only to make the overlapping same-cycle images align seamlessly, but to make the elevations of pass-points calculated from stereo agree with the elevations from altimetry. The question therefore arose of how sensitive the adjustment process is to artifacts in the Magellan altimetry used as a constraint. Elevations of individual altimeter footprints can be in error by several kilometers at high-contrast boundaries in the surface scattering function. Would the control process yield stereo DEMs that are similarly in error? This seemed unlikely in principle, because the adjustable parameters (position and velocity on 3 axes) allow each image to be translated and rotated as a whole, but not to be "warped" to fit erroneous altimetry data. Pass-points with bad altimetric elevations should therefore have large residuals as well, and it should be possible to identify them as outliers or "blunders" and exclude them from the solution as long as they are rare compared to good points. We nevertheless sought an external check for the reliability of our stereo DEMs.

The most direct verification of our results would be a comparison of our DEMs with independent, non-Magellan derived elevation data. Unfortunately, the best Earth-based elevation dataset for Venus, derived from Goldstone radar observations [17], was insufficient to address the potential errors inherited from Magellan altimetry. Only three altimetric observations by the Goldstone radar overlap with the Magellan stereo coverage. The nominal resolution of these DEMs is 1 to 5 km horizontally and 15 to 60 m vertically but they are dominated by artifacts and noise with a standard deviation of 1 km or more. It is difficult, if not impossible, to identify known topographic features in these DEMs. In addition, the data are not tied precisely to the Magellan coordinate system. We therefore did not attempt to map the corresponding regions in order to compare our results to the Goldstone DEMs.

Better Mapping Through Chemistry: A more indirect approach to validating our results was therefore needed, one that does not require a DEM from another source. The temperature- and therefore elevation-dependence of radar backscatter properties on Venus provide such a check. Low-reflectivity lowlands give way to extensive bright highlands, with a few of the highest elevations once again radar-dark. The lower transition occurs over a relatively broad range of elevations locally and at a height that varies by several kilometers globally. The upper transition is noticeably sharper and was therefore selected for test mapping. In particular, we mapped the portion of central Ovda Regio from 88-98E longitude, 8-5S latitude (Figure 1), which contains several high-elevation dark regions. One of the dark regions on the eastern side of the study area has previously been described by Arvidson et al. [18] who constructed DEMs of a portion of it from the same Magellan stereo data we used, but used different

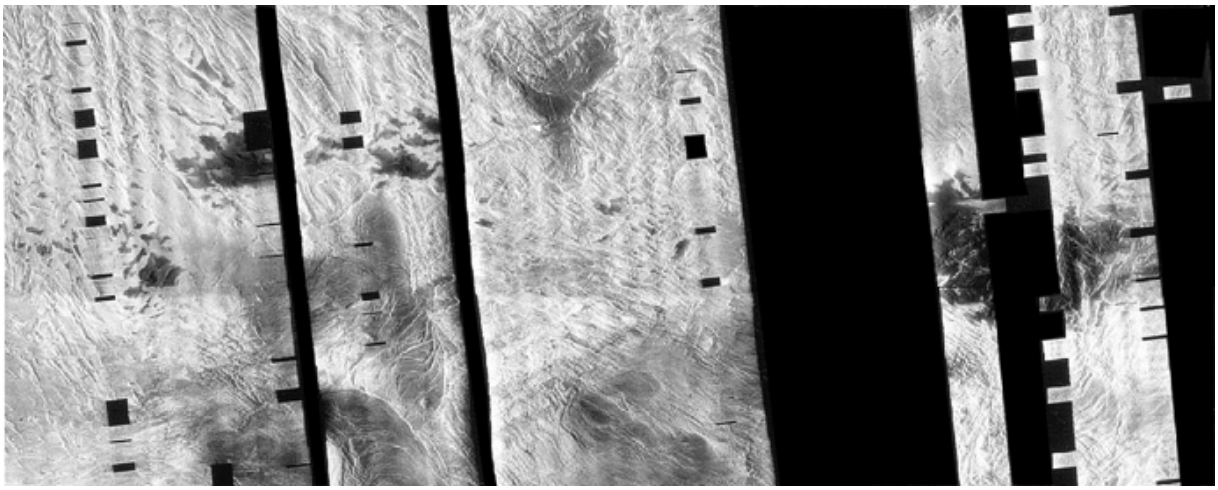

Figure 1. Portion of central Ovda Regio selected for topographic mapping tests. Boundaries of dark patches indicate thermochemical transition that should occur at near-constant elevation. Region is 88-98E longitude, 8-5S latitude. Data are taken from Cycle 3 (stereo look angle) C1-MIDR photoproducts. Not all orbits seen here were included in FMAP mosaics or could be found in F-BIDR archives, so area stereomapped (Fig. 2) is less complete.

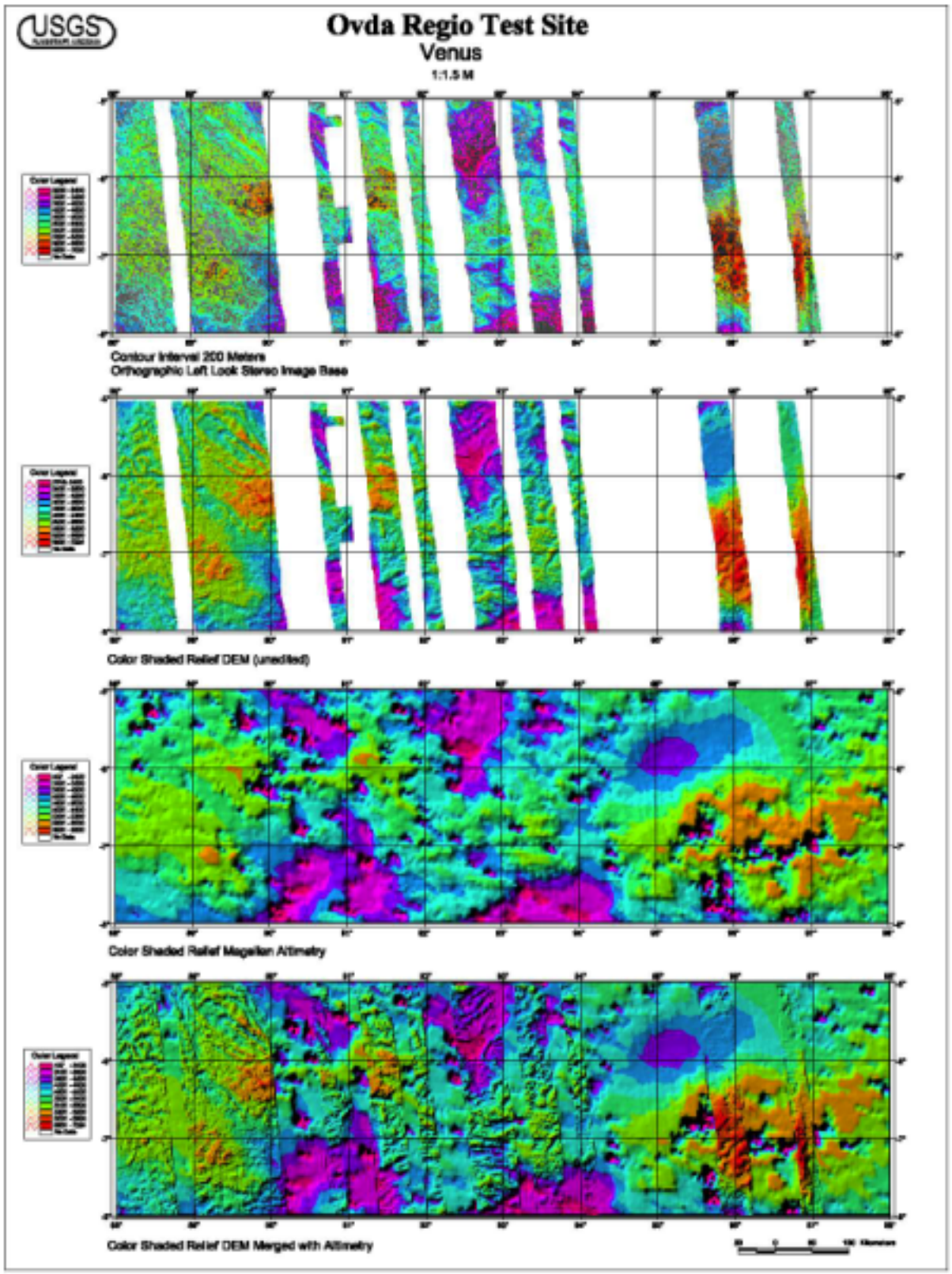

Figure 2. Digital Elevation Models (DEMs) of region shown in Figure 1. From top to bottom: contours (unequal intervals) from stereo-derived DEM superimposed on image base; color-coded shaded relief computed from stereo; color shaded relief from Magellan global gridded altimetry dataset (GTDR); stereo data merged with altimetry. Stereo data were collected at 675 m (9 pixel) post spacing, whereas altimetry footprint size is >10 km and track spacing is ~25 km. Altimetry dataset also contains prominent errors (e.g. near -7° lat, 95°–97° lon) in the form of incorrect low elevations ("pits") near boundaries of radar-dark patches. These errors are not reflected in stereo DEM because erroneous altimetry data were identified and excluded from bundle-adjustment calculation.

mapping software. An important result of their mapping was that the transition in emissivity and reflectivity takes place over an elevation range of 500 m or less. If our methods are valid, our DEM should indicate a similarly narrow range of elevations for the transition. In contrast, the Magellan altimetry dataset does not. The high contrast of the backscatter boundary in this area leads to severe (and geologically quite implausible) local variations in the altimetric elevations.

Images (F-BIDRs) used for our mapping came from 47 Cycle-1 orbits in the range 0947-0994 and 34 Cycle-3 orbits in the range 4536 to 4582; some images present in the Magellan Mission C1-MIDR mosaics were not used because they were not present in the USGS FMAP or because data were missing from the archive of F-BIDRs. Control points, 212 in all, were interactively measured between neighboring images of the same cycle, and between overlapping Cycle-1 and Cycle-3 images where possible. Because of gaps in the Cycle-3 data, it was not possible to connect all images by points that could be measured on both cycles (i.e., in stereo). Elevations of the control points were constrained based on the Magellan altimetry, and a least-squares bundle-block adjustment of the spacecraft ephemerides was performed to minimize the image-to-image and control-to-altimetric-elevation discrepancies. In this adjustment, constant offsets in the three orthogonal directions (along-track, across-track, and radial) were applied to the spacecraft orbit arc for each image. Higher-order deformation of the orbits was not modeled. As expected, altimetric elevations inconsistent with the remainder of the altimetry data and the stereoimagery were readily identifiable because they produced large elevation residuals. Control points found in this way to be tied to unreliable altimetry data were eliminated from the final control solution. Where possible, they were replaced by control points nearby for which elevation residuals were found to be acceptable. After a satisfactory control solution was obtained, DEMs were collected by automatic stereomatching of each overlapping stereopair of images. A bare minimum of interactive editing was done to correct spikes in a few areas where the automatic matcher failed, and the DEM segments were merged and used to derive the map products shown in Figure 2.

A closeup of our contour data (Figure 3) for the region mapped by Arvidson et al. [18] shows that the margin of the dark regions varies locally in elevation by <200 m for considerable distances. The elevation of the bright-dark transition varies by a maximum of 500 m across the entire region we mapped, and considerably less across the region also mapped by Arvidson et al. [18], leading us to speculate that the 500-m height range that they reported for the transition might have been exaggerated because of the low spatial resolution of the emissivity measurements they used. A few areas on the right of Fig. 3 that appear dark but are several hundred meters lower are probably unrelated to the reflectivity change with altitude. They appear smooth at the resolution of the image, and, if they are also smoother than their surroundings at the scale of the radar wavelength, this would explain their dark appearance.

In contrast to both our stereo-derived DEMs and those of Arvidson et al. [18], the Magellan altimetry for this area shows a series of apparent "pits" 20-50 km wide (i.e., one to a few altimetry footprints) and typically 3 km deep. A chain of such pits runs through the dark areas; if the altimetry were correct, some of the dark material would have to lie 3 km below the majority of the transition boundary. Furthermore, local

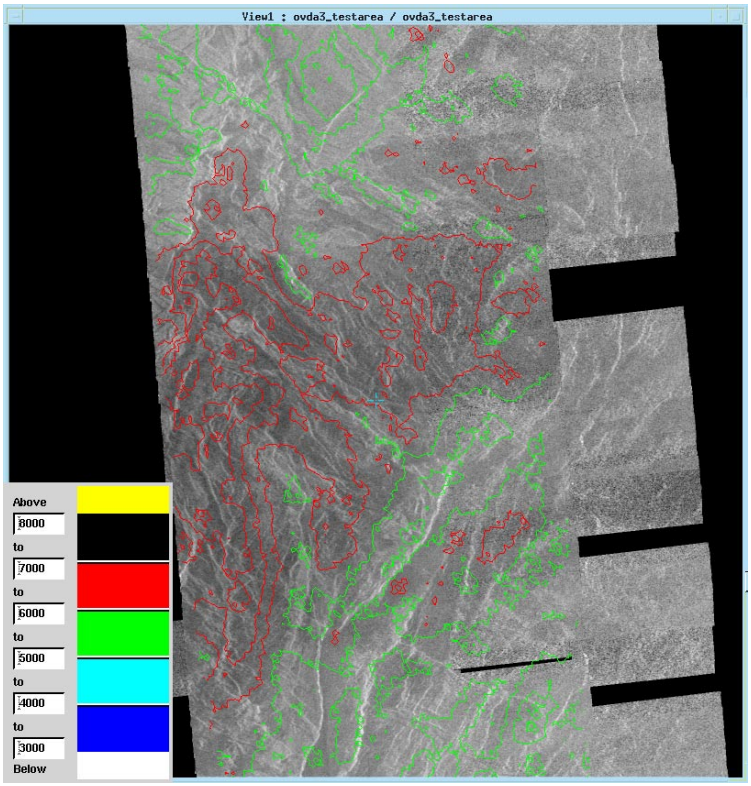

Figure 3. Closeup of contours derived from stereo DEM for part of the region shown in Figs. 1–2, centered near -7° lat, 96° lon. Contour interval is 250 m, with contours colored by absolute elevation as shown. Elevation along boundary of largest dark patch is constant to <200 m; Arvidson et al. [18] limited the range of boundary elevations to <500 m based on uncontrolled stereotopographic mapping. Figs. 3–4 contain data from an additional stereo orbit not used in Fig. 2.

slopes of as much as 15 degrees would be implied; there is no morphologic evidence for such slopes in the images or for any visible peculiarity spatially associated with the altimetry lows. We conclude that these low elevations are artifacts resulting from noisy or incorrectly interpreted altimeter echos. Fortunately, the vast majority of the altimetry data are not subject to such severe errors, so it is possible to constrain the stereogrammetric control solution to follow the altimetric DEM where it is valid and robustly exclude bad altimetry datapoints from the control solution.

Statistical Comparison of DEMs: To compare our results with those obtained by Arvidson et al. [18] first required generating additional DEM data using Cycle-3 orbits 4581 and 4582. (Note: orbits 4581 and 4582 were not present in the USGS F-MAPS because these data are missing from the archive of F-BIDRs at the USGS. We obtained the missing orbits from the Washington University CD-ROM archive.) Once we generated the needed DEM results, we compared the datasets and found them in reasonable visual agreement except for (a) absolute elevation, (b) horizontal position, and (c) grid spacing. These discrepancies are directly attributable to the differences in software, datasets, and methodologies used. Arvidson et al. used the Magellan Stereo Toolkit software to extract their DEM and used the spacecraft ephemerides available during the Magellan mission without adjustment (i.e., their DEM is uncontrolled). In contrast, we started with the improved Konopliv ephemerides and performed a local bundle-block adjustment to insure agreement between the stereo elevations and selected altimetry points. We also chose a DEM grid spacing of 675 m, almost twice as fine as the 1200 m spacing used by Arvidson et al. Note that our software provides the option of using even finer grid spacing at the

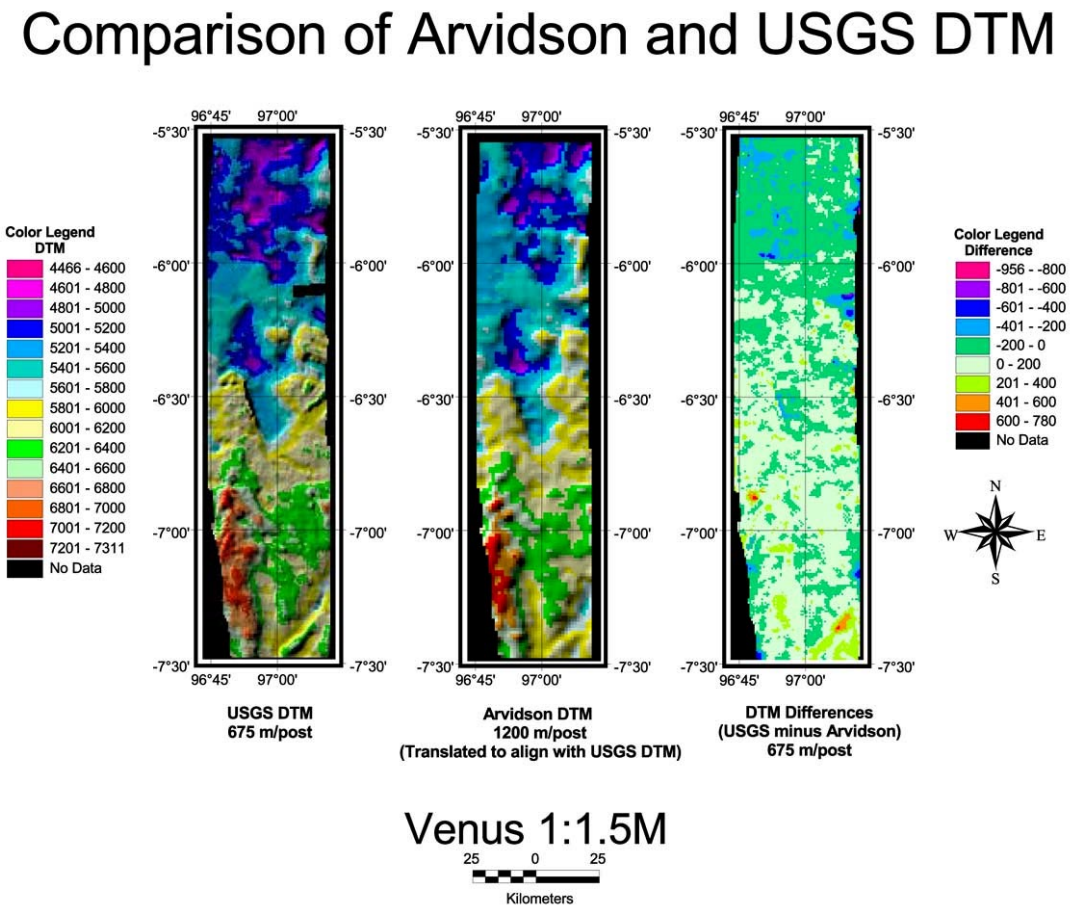

Figure 4. Comparison of USGS stereo-derived DEM of central Ovda Regio with that of Arvidson et al. [18]. Region covered is approximately the same as in Fig. 3. Arvidson DEM (center) has been resampled to resolution and position of USGS DEM at left. Right panel shows difference between USGS and adjusted Arvidson DEMs; note color scale differs from that used for the individual DEMs. Root-mean-squared difference between DEMs is 128 m, reflecting mainly a net tilt of the controlled USGS DEM relative to the uncontrolled dataset. Minor differences resulting from the lower intrinsic resolution of the Arvidson DEM are also visible. Neither DEM contains the "pit" errors seen in Magellan altimetry in this area (Fig. 2).

expense of additional computation time. A practical lower limit for independent elevation measurements is 225 m, corresponding to a 3-pixel matching window. DEM posts can be placed closer together than this but smaller topographic features will not be resolved.

To bring the datasets in horizontal and vertical agreement, we translated the Arvidson DEM by -0.07979° (~8 km) in longitude, +0.0186252° (~2 km) in latitude, and -1337.6 meters in elevation. (The stated elevation change is in addition to 1000 m correction of the represented value to our datum radius of 6051 km. Arvidson et al. used a radius of 6050 km for their zero-elevation surface, so 1 km must be subtracted from their data to reference them to 6051 km.) This translation was accomplished using the DEM Registration tool in SOCET Set. For meaningful qualitative analysis, we additionally resampled the Arvidson DEM to increase its resolution from 1200 m/post to 675 m/post and edited out bad data at the edge of the Arvidson DEM.

The magnitude of the needed translations in latitude and elevation are reasonable, based on the uncertainties in the mission ephemerides used by Arvidson et al., though the longitude shift is somewhat large. The estimated uncertainties along- and across-track for Cycle 1 orbits in this area are close to 2 km. The along-track uncertainty for Cycle 3 is also about 2 km but the across-track uncertainty is only 0.7 km. The radial uncertainties are much smaller, around 10 meters; the vertical offset of the DEM is mainly a parallax shift resulting from the separate adjustment of the Cycle 1 and Cycle 3 across-track.

With the two DEMs aligned and resampled to common resolution, we were able to make a statistical comparison of elevation values. The mean elevation difference was found to be -0.3 m (the negative sign indicating that USGS elevations were lower than resampled Arvidson elevations) and the standard deviation of the difference was 128.3 m.

Statistical comparison of the DEMs is complemented by visual examination of color-coded shaded relief maps and a color-coded map of the difference between the two DEMs after coordinate adjustment (Figure 4). Seen side-by-side, the two DEMs clearly show the same geologic features but the greater sharpness of the USGS product is evident. The difference map shows the local variations that are to be expected for datasets of different resolution, but also shows that part of the residual difference corresponds to a systematic north-south tilt of one DEM relative to the other. The USGS DEM is roughly 200 m lower relative to that of Arvidson et al. at the northern end of the mapped region than at the southern end, corresponding to a relative tilt of one part in 1000 (~0.06°). This relative tilt, like the overall elevation difference, results from the USGS bundle-adjustment bringing the stereomodel into agreement with the reliable altimetry data, i.e., it is a real effect. Adjustment terms for each image include velocities as well as offsets in the along-track, across-track, and radial direction; as a consequence, we can correct errors in position that vary linearly along the image as well as constant errors.

Conclusion: The most important conclusion of our comparison between the USGS and Arvidson et al. DEMs is that neither shows any sign of the multi-kilometer depressions seen in the altimetric DEM for this area (the Arvidson et al. DEM corresponds to the easternmost section of stereo data in Fig. 2). We were easily able to detect during our bundle-adjustment process that the altimetric elevations in the apparent depressions were inconsistent with the remainder of the data and therefore did not use these elevations as constraints in the calculation. The result of our bundle-adjustment with selective use of altimetry constraints and the other software and procedures we have developed is a high-resolution, stereo DEM that agrees well with altimetry in the regions of uniform reflectivity where it is reliable yet is not distorted by the altimetry artifacts where there are strong reflectivity contrasts. Magellan stereo images are available to make topographic maps of about 17% of Venus by this process. We have proposed to begin systematic mapping of the areas that combine high scientific interest with the most complete stereo coverage.

References: [1] Saunders, R. et al., (1992) *JGR, 97,* 13067-13090. [2] Leberl, F. et al. (1997) *JGR, 97,* 13675-13689. [3] Curlander, J and Maurice, K., (1993) *Magellan Stereo Toolkit User Manual* (unpublished). [4] Wu, S.C. et al., (1994) *LPS XXV,* 1519-1520. [5] Miller, S.B. and Walker, A. S. (1993) *ACSM/ASPRS Annual Convention and Exposition Technical Papers, 3, 256-263.* [6] Miller, S.B. and Walker, A.S. (1995) *Z. Photogramm. Fernerkundung, 1/95,* 4-16. [7] Eliason, E. (1997) *LPS XXVIII,* 331-332. [8] Gaddis, L. et al. (1997) *LPS XXVIII,* 387-388. [9] Torson, J. and Becker, K. (1997) *LPS XXVIII,* 1443-1444. [10] Kirk, R. L. et al.. (1999) *JGR, 104* (E4), 8869–8887. [11] Rosiek, M. R., et al. (2000) *ASPRS 2000 Proceedings*, (CD-ROM). [12] Rosiek, M. R., et al. (2001) Utilizing Mars Digital Image Model (MDIM) and Mars Orbiter Laser Altimeter (MOLA) data for photogrammetric control, this conf. [13] Kirk, R. L., et al. (2001) High resolution digital elevation models of Mars from MOC Narrow Angle stereoimages, this conf. [14] Howington-Kraus, E., et al. (2000) *LPS XXXI*, 2061. [15] Rappaport, N.J. et al. (1999) *Icarus, 139,* 19-31. [16] Chodas, P. et al., (1993) *AAS/AAJA Astrodynamics Specialist Conference,* (accessed at http://techreports.jpl.nasa.gov). [17] Jurgens, R. F., et al. (1980) *JGR, 85*, 8282-8294. [18] Arvidson, R. et al. (1994) *Icarus, 112*, 171–186.